A Directed Graph Neural Network Approach to Understanding Battery Degradation Mechanisms in NCA Cells

Matthew A. Clarke* and Patrick Herring†

Toyota Research Institute - Advanced Materials Design & Discovery, Cambridge, MA 02139

The application of graph neural network theory for quantifying the degradation mechanisms that contribute to capacity fade and internal resistance growth within lithium-ion battery cells during aging is presented in this paper. The structure of the graph neural network is based on literature detailing physical-chemical phenomena and processes occurring during repeated cycling. The construction of this neural network which maps environmental and operating conditions to the most prevalent degradation stress factors to degradation is documented to demonstrate its applicability to other battery chemistries. Preliminary results show mixed success, with the model being able to capture some expected trends with the cycle but now over the during of aging. Lastly, we identify future tests to maximize information in the design space to shorten testing.

I. Introduction

In this study, we seek to understand trends in the stored energy capacity and available power of a battery as the performance degrades with time and repeated cycling. Such long-term projections can be collectively termed state of health estimation. Accurate estimation of remaining useful life is crucial for the battery online management in electrical vehicles as well as secondary applications such as grid storage. As Han writes, *"considering the nonlinear fading characteristics of the battery, the conventional extrapolation method cannot accurately predict the remaining life of the battery."* It therefore becomes important to forecast performance *"based on the dominant aging mechanism and corresponding battery life under various working conditions and different fading stages"*. This research proposal centers around an in-depth understanding of the major types of degradation mechanisms: Solid-electrolyte interface (SEI) layer growth; Loss of anode/cathode active materials (LAM); Loss of lithium-ion inventory (LLI); Loss of Electrolyte (LE); Lithium corrosion; Lithium plating; Contact loss and Diffusion Stress. The ease and extent to which lithium intercalation and deintercalation occurs on the anode and cathode directly governs the battery's charging and discharging characteristics. This in turn governs the battery's stored energy capacity, abbreviated battery capacity in this paper. Additionally, structural deterioration, phase changes and electrolyte depletion within the cell inhibit the movement of charged particles leading to an increase in internal resistance. A more detailed account of how these degradation mechanisms contribute to changes in performance will be expounded on in the following sections.

The development of an empirical representation of these aforementioned degradation processes may be a more pragmatic approach for system modeling, but is insufficient information to achieve inverse battery design, which is the process of guiding battery design by the desired behaviour. On the other hand, more mechanistic methods require fitting and tuning hyperparameters either through some form of nonlinear regression or neural network. The drawback to such approaches is that they can be ill-suited for battery management system operation. As a result, a combination of high-level operation data and lower-level mechanistic behaviour theory is utilized in this study to provide a fast but accurate estimation of the discharge and charge dynamics of the cell.

The cells examined in this study are commercial Lithium Nickel-Cobalt-Aluminum Oxide (NCA) cells. The primary elements of this cell are a layered-spinel-rock salt cathode, crystalline allotropic form of carbon (graphite) anode and a liquid organic solvent containing free ions and other compounds for fire retardation and decelerating the formation of unwanted by-products. This type of cell has a usable charge storage capacity of 180 to 200 mAh/g [1], well below the theoretical values of 279 mAh/. However, this is significantly higher than that of alternative materials such as Lithium Cobalt Oxide (LCO) with 148 mAh/g, Lithium Iron Phosphate (LFP) with 165 mAh/g and Lithium Nickel Manganese Cobalt Oxide (NMC) with 170 mAh/g [2]. Additionally, NCA has excellent fast charging characteristics, making it tractable for electric vehicle (EV) applications.

---

*Ph.D. Candidate, Department of Aeronautics and Astronautics
†Senior Research Scientist, TRI-AMDD

II. Approach Philosophy

The cascading and highly coupled nature of reactions within the cells makes discerning the root cause of a particular observation during diagnosis testing a nontrivial task. In addition to changes in state and composition of the electrodes and electrolyte, particle transfer induces stresses at interfaces which over time succumb to strain, resulting in additional reactions and the formation of unwanted byproducts as with tine chase of SEI growth. Each of the primary components of the cell themselves has its respective chemical and mechanical properties which can vary with environmental conditions such as temperature. Battery degradation is therefore still an active research topic. Some studies opt for a more theoretical approach to modeling degradation in which the loss of active materials [3–8]. Others attempt to link a theoretical approach with the experimental cycling schedule to directly correlate charging and discharging patterns with molecular level processes occurring within the cell [9, 10]. On the opposite end of the spectrum, empirical models that adopt an operational and cell performance level have been proposed and implemented by [11–15]. These models however are constrained by the quantity and quality of the experimental data which can be time-consuming to obtain.

The approach taken in this study leverages elements of the theoretical approach to identify internal processes and couples data obtained by an extensive experimental campaign to validate measurable parameters. It draws parallels to disease diagnosis, where external agents such as harmful air particulates and viruses can induce responses of the human immune system causing the body to have an adverse reaction. These reactions are observable and provide us with an idea of the defensive biological processes occurring within the body. For example, pollen (external stimulus) is a well-source of allergic reactions (biological process). The ensuing irritation to the olfactory system results in inflamed sinuses (phenomenon expression) that can manifest externally (observation) as a runny nose, itchy eyes and sneezing. In Figure 1 illustrating this process, we can infer that the easily observed parameters are the external stimuli and the observations while the physical-chemical processes and phenomena expressions can be said to be unobserved due to their difficulty to be accessed. That being said, though the latter two parameters are difficult to examine, advanced techniques in pathology enable us to make connections of the stages and allow the administering of the most appropriate treatment. In the study, we consider the battery akin to the human body, whereby there are parameters that are both observed and unobserved. Again, must be noted here that the distinction of whether a variable is observable and unobservable refers to the ease of measurement. For example, the temperature of a battery cell and electrical load can be quickly and inexpensively measured using thermocouples and ammeters respectively. On the other hand, despite internal features of the electrochemical cell such as the size of the SEI layer and cracks at the electrode-electrolyte interface can hypothetically be measured, it requires the delicate dissection of the cell which can sometimes cause damage to the same surface one is trying to inspect. This undertaking is often very slow and expensive imaging techniques. Provided in the following section is a thorough overview of these four stages which will be used as the basis for the deep learning models proposed in the following section.
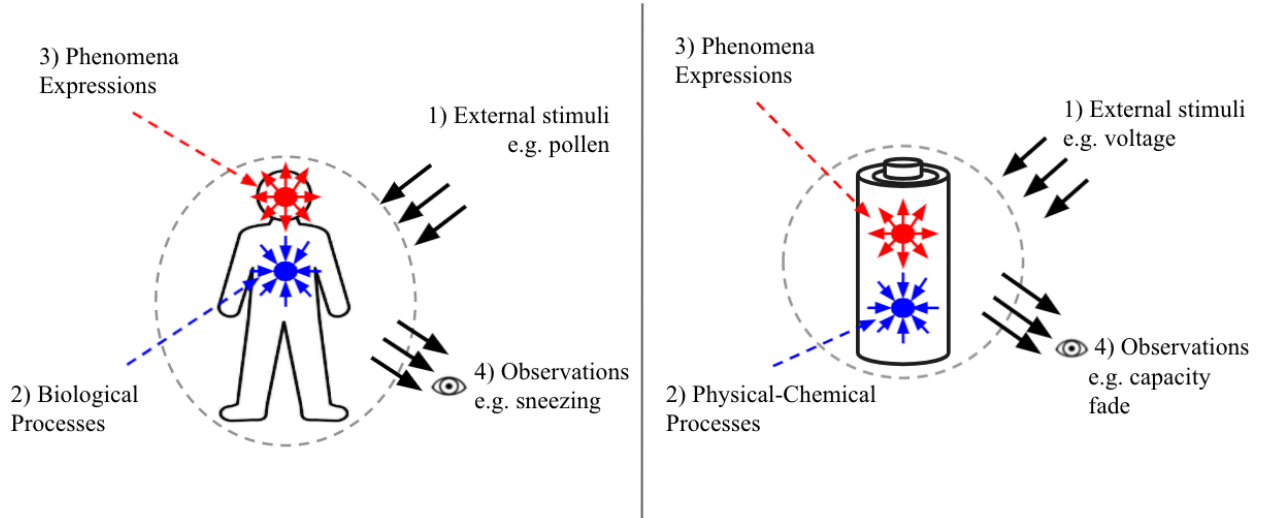

Fig. 1 **Battery capacity fade and possible internal mechanism in different stages.**

Stage 1: External Stimuli

In the context of a battery degradation, external stimuli encompass operating conditions of the cell cycler and environmental conditions measurable by instrumentation. They include variables such as battery temperature, the number of cycles, as well as cell voltage, current loads and state of charge. These stimuli are aggregated in Table 1 for completeness, and again in Table 2 where their respective relationships with other internal processes are documented. Since stimuli are the starting point of the degradation process, they do not have inputs, but rather contribute to the physical-chemical changes within the cell and thus the corresponding entries in the output column are given.

Stage 2: Physical-chemical Processes

During charging, the density of lithium within the cell changes considerably as lithium ions move from the cathode to the anode. Conversely during discharge, lithium ions move from the anode to the cathode. The movement of charged particles and associated side reactions is accompanied by the flow of electrons outside of the cell to an external load. Han [16] suggests that the aging in lithium battery cells of three regions as shown in Figure 2. In the first stage during the first few charging cycles, there is a rapid decrease in battery capacity due to a LLI, specifically the formation of the SEI on the anode. The second stage consists of the steady decrease in performance due to the various aforementioned degradation mechanisms occurring within the battery. The final stage is characterized by a rapid drop in battery capacity as a result of either significant lithium-ion inventory loss due to lithium deposition [17, 18] and/or the active material loss due to a depleted electrolyte [19]. This point is often referred to as the "knee" point due to its distinctive shape.

Though the major classifications of degradation mechanisms provide a means of grouping internal processes, they are insufficient for any meaningful prognosis of the components which make up the cell.

Fig. 2 Battery capacity fade and possible internal mechanism in different stages. [16]

The further breakdown of degradation mechanisms in processes by Vetter et. al [6] therefore serves as the foundation upon which we examine cells in greater detail. Specific to the NCA-based cathode used in this study, the loss of oxygen during cycling causes phase transitions to occur [20, 21]. According to a review by Fang [22], *"the oxygen intermediates on the surface are rapidly depleted by the electrolyte solvents, and the oxygen evolution processes inside the cathodes are more kinetically hindered"*. As a result, the layered-spinel-rock salt phase transition is much more severe near the surface of particles and cracks than that in the bulk of the cathodes. This is accompanied by the chemical oxidations of electrolyte solvents casing gas generation leading to an increase in volume at the interface of the cathode and organic solvent, the best case of which is separation at the interface, the worse case in the onset of an explosion of the self-containment of the cylindrical canister. During cycling, the volume of the graphite anode changes by as much as 10% due to the insertion and extraction of lithium ions [6, 23]. This volume change can cause the SEI film between the anode and electrolyte first developed during the first few cycles to crack, resulting in lithiated graphite once again coming into direct contact with the reactive electrolyte [24, 25]. This repetitive process results in the continuous consumption of the lithium inventory and thickening of the SEI film, resulting in a steady decrease in the amount of lithium-able facility at the moment of charge in the external circuit, leading to a decrease in performance. This formation and continuous thickening of the SEI film on the surface of graphite anode is widely accepted as one of the major reasons for lithium-ion battery aging [26, 27]. An even more thorough breakdown of the physical-chemical processes are provided in Table 2
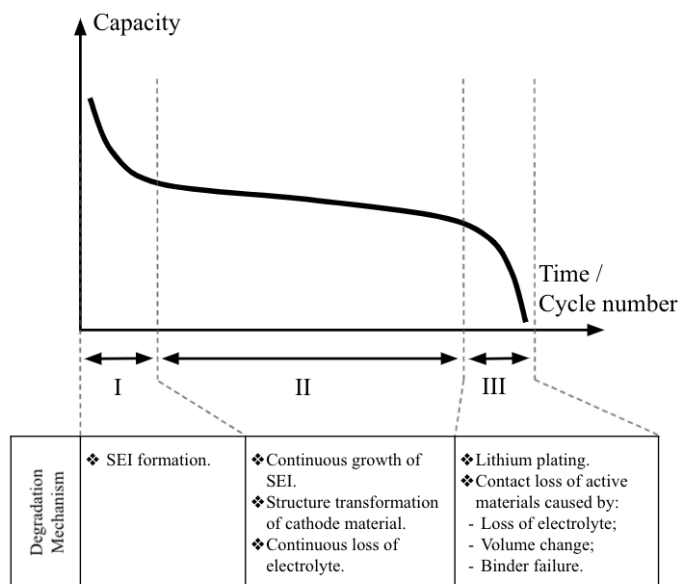
Stage 3: Phenomena Expressions

Physical-chemical processes occurring within the cell during each cycle manifest a variety of ways from the creation of undesired byproducts at the interface of two adjacent media to irreversible state changes. In this study these are referred to as phenomena expressions and serve as the intermediary stage between the physical-chemical processes and the observed variables. For example, thermal instabilities of NCA due it is high nickel content of lead to changes in its crystal structure with increasing temperature resulting in oxygen gas production followed by an exothermic reaction between oxygen and electrolyte, which further accelerates the decomposition of the cathode and finally facilitates thermal runaway [28]. We can define this gas production as a phenomena expression as it is a direct result of a physical-chemical process. A second example is at the interface between the anode and cathode where the decomposition of the conducting salt LiPF6 causes an increase in fluorine in SEI. These electrolytic reactions would therefore be considered a phenomena expression, while the thickening of the SEI layer is an example of a phenomena expression. We refer to the reader to Table 2 for a more detained summary.

Stage 4: Observations

Similar to the first stage, this final stage can be easily quantified using instrumentation and diagnostic techniques. This includes the cell's impedance, which arises from the loss of electrolytes, contact resistance, and SEI film resistance. Other observations include charge and discharge energy as well as charge and discharge capacity, which together with voltage can be used to acquire the incremental capacity (IC) curves. These curves track an electrochemical system's capacity increase upon charge or decrease during discharge, shedding light on the underlying thermodynamics and kinetics of the system. The IC curve is obtained by differentiating the capacity vs. voltage and is typically plotted vs. voltage or charge. The advantage of the IC curve is that plateaus associated with phase transformations of the electrode material in the voltage (V) vs. charge(Q) charge curve can appear as clearly identifiable peaks in the dQ/dV vs. V curve. Again, a full list of all observations used in the construction of the graph neural network (GNN) is provide in Tables 1 and 2.

Table 1   Battery Degradation Mechanisms.

Table	Classification	Parameter/GNN Node	Acronym/Node Label
	External Stimuli	Age/No of Cycles	A
	External Stimuli	Current	C
Stage 1	External Stimuli	State of Charge	SOC
	External Stimuli	Temperature	T
	External Stimuli	Voltage	V
	Physical-Chemical Process	Cathode Phase Transition	CPT
	Physical-Chemical Process	Cathodic Mixing	CM
	Physical-Chemical Process	Electrolyte Reactions	ER
	Physical-Chemical Process	Flouride Composition Change	FCC
Stage 2	Physical-Chemical Process	Lithium Concenturation in Cathode	CLC
	Physical-Chemical Process	Nickel Concentration in Cathode	CNC
	Physical-Chemical Process	SEI Chemical Composition Change	SEICCC
	Physical-Chemical Process	Solid Electrolyte Interface Lithium Concentration	SEILC
	Phenomena Expressions	Cathode Gas Production	CGP
	Phenomena Expressions	Cathode Interclation	CI
	Phenomena Expressions	Cathode Interfacial Cracks	CIC
Stage 3	Phenomena Expressions	Electrolyte Decomposition	ED
	Phenomena Expressions	Heat Generation	HG
	Phenomena Expressions	Solid Electrolyte Interface Growth	SEIG
	Observation	Charge Capacity	CC
	Observation	Charge Energy	CE
Stage 4	Observation	Discharge Capacity	DC
	Observation	Discharge Energy	DE
	Observation	DVDQ Curve	DVDQ
	Observation	Internal Resistance Growth	IRG

**Table 2   Relationships and inter-dependencies of processes occurring within the cell.**

No.	Process	Node Label	Caused by	Leads to
1.	Temperature variations	T		CPT,SEIFC,ER SEILC
2.	Voltage variations	V		CM,CPT
3.	Current variations	C		CPT
4.	Battery cell SOC	SOC		CM,SEIFC,SEILC
5.	Battery age/number of cycles	A		SEIFC,SEILC
6.	A reduction in cathode interclation inhibits the kinetics of Li diffusion and increases the cell impedance, leading to a practical capacity loss. [29]	CI	CIC	IRG,CE,DE CC,DC
7.	The layered-spinel-rock salt phase transition is more severe near the surface of particles resulting in cracks. This is accompanied by chemical oxidation of the electrolyte resulting in gas generation. [22]	CIC	ER	CGP
8.	The phase transformation of the cathode is strongly related to the Li content in the cycled LixNiO2 electrode. [29]	CLC	CPT	CI
9.	During cycling, Ni2+ ions migrate to the Li+ ion layer and occupy the locations of the Li+ ions resulting a phase change. [22]	CM		CNC,CLC
10.	Ni/Li mixing can be attributed to thermodynamic instability of the cathode induces the reduction of Ni3+ to Ni2+ and leads to a net loss of Li and O in the form of Li2O and O2. [22]	CM	T	CI.
11.	NCA suffers from thermal instabilities that lead to changes in its crystal structure from the layered phase to the spinel phase to the rock-salt phase with increasing temperature. It is accompanied by a small amount of oxygen release followed by an exothermic reaction between oxygen and electrolyte, which further accelerates the decomposition of the cathode. This phase transformation also results in volume changes that induce microcracks in the cathode. [28]	CPT	T	ER,CGP,CI, HG, CIC
12.	Layered-spinel-rock salt phase transition is the inevitable result of the cationic mixing, which causes the loss of oxygen from the NCA cathodes. The oxygen intermediates on the surface are rapidly depleted by the electrolyte solvents, and processes inside the cathodes are more kinetically hindered. [22]	CPT,CLC,CNC	CM	CGP,ER
13.	SOC significantly affects both the structural changes and the evolution of oxygen as the temperature increases: the more extensive the charge, the lower the temperature of the phase transitions and the larger the oxygen release. [28]	CPT	SOC	CGP
14.	Material loss caused by the dissolution of the transition metal directly cause the cathode capacity and anode capacity to fade.	CLC	CPT	CI,ER
15.	Electrolytic reactions are exacerbated by graphite anode exfoliation and cathode corrosion, leading to electrolyte and binder decomposition coupled with SEI thickening.	ER	V,C,SOC,A	ED,SEIG
16.	Increase in impedance is caused by replacement of carbonic SEI components over time, e.g.,Li2CO3 with fluoridic ones such as LiF.[30]	SEIG	SEILC,CLC, SEIFC,ER	IRG
17.	Fluorine and Lithium in SEI layer increases with temperature and number of cycles, resulting in the decomposition of the electrolyte and the enrichment of the SEI. [30]	SEIFC, SEILC	A,T,ER	ED
18.	Side reactions at the graphite/electrolyte interface cause electrolyte consumption and decomposition. As the SEI film become thicken, cell impedance increases.[30]	SEIG	ED	IRG,CE,DE CC,DC
19.	Changes in cell internal resistance	IRG	CI,SEIG	
20.	Changes in cell charge energy	CE	SEIG,CI,ED,CIC, HG	
21.	Changes in cell discharge energy	DE	SEIG,CI,ED,CIC, HG	
22.	Changes in cell charge capacity	CC	SEIG,CI,ED,CIC, HG	
23.	Changes in cell discharge capacity	DC	SEIG,CI,ED,CIC, HG	
24.	Changes in cell the incremental capacity curve	DVDQ	CIC,CI,DC, CC	

III. Graph Neural Network Construction

A temporal graph neural network (GNN) was chosen to learn how the degradation mechanisms described in the previous section behave over time and interact with one anther. This was made possible using the Pytorch Geometric-Temporal [31] library, and extension of the Pytorch Geometric [32] library which is itself built upon Pytorch [32]. A GNN is made up of nodes where each node has a state or target, y, and attributes $\mathbf{x}$, otherwise referred to as features. Pytorch Geometric-Temporal employs a rolling window approach to chronologically define past targets of a node as its features. The user is able to specify the size of this window, which is also referred to as a lag. This type of neural network is advantageous to this time of problem for the following reasons:

- A graph neural network allows us to explicitly prescribe relationships between nodes. This enables us to take advantage of background knowledge and prior research to guide the behaviour of the nodes when training the network.
- A graph neural network allows the user to quickly vary the strength of a connection between nodes or in extreme cases, add and remove any relationship
- The chronological nature of how node features are defined removed the need for node features to include information about battery cycle time or age, reducing the number if training parameters
- A temporal network allows for "fading memory" whereby the impact of operating conditions which result in a particular node target in the distant past do not have a significant impact on the prediction of future targets. This is an important feature when examining battery cells in a test stand, whose test conditions change over time, or in more realistic circumstances, battery cells in a drive train of an electric vehicle.

Temporal GNNs have been used for a variety of regression, classification and spatiotemporal forecasting problems. For example, Panagopoulos et. al [33] employed graph neural networks to predict the number of future cases of COVID-19. In their model, where nodes represented a country's regions and the edge weights denote human mobility across regions. Diffusion patterns that govern the spread of the virus were encoded into the learning model. Another example is traffic forecasting as demonstrated by Li et. al [34]. This study, a directed graph trained on a traffic dataset comprising a network of 325 traffic sensors in the Bay Area with 6 months of traffic readings. This dataset was collected by California Transportation Agencies (CalTrans) Performance Measurement System (PeMS). In this study, we utilize a GNN to determine the behaviour of unobserved processes where cross validation is not possible due to the lack of data. The model is however pinned down training on observed nodes, notably external stimuli (red) and observations (green) nodes. As a result, one major assumption that the authors make is that outside the trends described in 2, learned trends of the nodes follow the behaviour within the cell during repeated cycling. With that being said, the validity of using such an approach would be further strengthened through additional information of blue and yellow nodes.
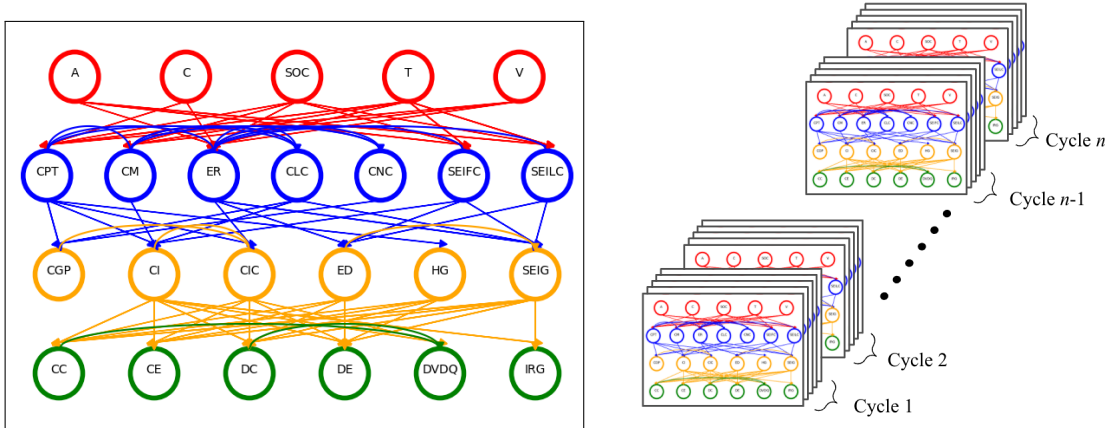
(a) A single directed graph representing one temporal snapshot.

(b) Temporal snapshots grouped by cycle.

Fig. 3   Directed Graph Structure.

The parameters listed in Table 1 can be visually represented in the graph structure in Figure 3a. The nodes are colored by classification for ease of interpretation. A collection of nodes and directed edges sharing the same time step can be represented as a graph, G. These graphs can be arranged in temporal snapshots i.e. $G(1), G(2) \dots G(T)$, which can be further grouped into cycles as shown in Figure 3b. Snapshots consist of node targets as shown by the red arrow

whereas dotted red lines represent the features as shown in Figure 4a. At each successive time-step, the window is updated to a future state. Message passing over the network is mathematically formulated in Equation 1. If we represent the weight of a directed edge from node a to node b as $w_{a,b}^{(t)}$, we can construct an adjacency matrix, $\mathbf{A}$, that defines the relationship between all nodes in a graph $G(t)$. Here, $\mathbf{A}$ is the vector of node attributes such $x_a^{(t)} = (c_a^{(t-n)}, ..., c_a^{(t)}) \in \mathbb{R}^s$, which contains previous values of the node over the past s snapshots, otherwise referred to as the lag. The process is repeated until the model reaches the end of the training set.

(a) Snapshot 1.

(b) Stapshot 2.
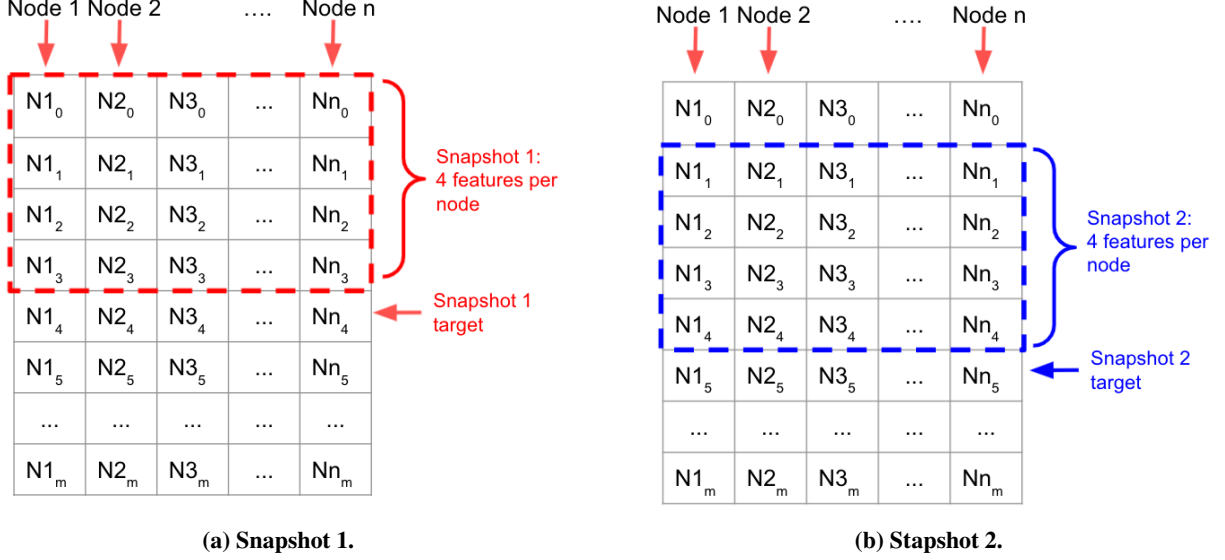
Fig. 4   First and second stapshots.

$$\mathbf{A}^{(t)}\mathbf{X}^{(t)} = \begin{bmatrix} w_{1,1}^{(t)} & w_{2,1}^{(t)} & \cdots & w_{n,1}^{(t)} \\ w_{1,2}^{(t)} & w_{2,2}^{(t)} & \cdots & w_{n,2}^{(t)} \\ \vdots & \vdots & \vdots & \vdots \\ w_{1,n}^{(t)} & w_{2,n}^{(t)} & \cdots & w_{n,n}^{(t)} \end{bmatrix} \begin{bmatrix} \mathbf{x}_1^{(t)} \\ \mathbf{x}_2^{(t)} \\ \vdots \\ \mathbf{x}_n^{(t)} \end{bmatrix} = \begin{bmatrix} \mathbf{z}_1 \\ \mathbf{z}_2 \\ \vdots \\ \mathbf{z}_n \end{bmatrix} \tag{1}$$

Due to the size of the raw battery cycling data, the dataset is first coarsened but taking a percentage, η. This serves two purposes: first, it reduces computation time during learning; secondly, the reduction in sensitivity of measurements work in our favor by serving as a preprocessor that identifies the major trends in the dataset. There is a lower limit to coarsening however, as too low a resolution will not not capture the trends of a particular parameter within each cycle, for example the SOC curve during charging and discharging. In this study $\eta = 0.02 - 0.05$ sufficiently of captured features of the data in each cycle. A Message Passing Neural Network with Long Short Term Memory (MPNN-LSTM) is used for training the model. These networks consist of a series of neighborhood aggregation layers. Each layer uses the graph structure and the node feature vectors from the previous layer to generate new representations for the nodes. Similar to [33] , the representations of the vertices of each graphs is updated following neighborhood aggregation scheme:

$$\mathbf{H}^{i+1} = f\left(\tilde{\mathbf{A}}\mathbf{H}^i\mathbf{W}^{i+1}\right) \tag{2}$$

where $\mathbf{H}^i$ is a matrix that contains the node representations of the previous layer, with $\mathbf{H}^0 = \mathbf{X}$, $\mathbf{W}^i$ is the matrix of trainable parameters of layer i, and f is the non-linear Tanh activation function. Given a model with K neighborhood aggregation layers, the matrices $\tilde{\mathbf{A}}$ and $\mathbf{H}^0, \ldots, \mathbf{H}^K$ are specific to a single graph, while the weight matrices $\mathbf{W}^1, \ldots, \mathbf{W}^K$ are shared across all graphs. This These representations are then fed into a two layer LSTM [35] network which capture the long-range temporal dependencies in time series. The mean squared error loss function defined in Equation 3 is used in the training of the model.

$$\mathcal{L} = \frac{1}{nT} \sum_{t=1}^{T} \sum_{v \in V} \left(y_v^{(t+1)} - \hat{y}_v^{(t+1)} \right)^2 \tag{3}$$

Here, $y_a^{(t+1)}$ denotes the update value the node at time step $t+1$ and $\hat{y}_a^{(t+1)}$ denotes the predicted value. Due to the size of the raw battery cycling data, the dataset was first coarsened but taking a percentage, η. This serves two purposes: first, it reduces computation time during learning; secondly, the reduction in sensitivity of measurements works in our favor by serving as a preprocessor that identifies the major trends in the dataset. There is a lower limit to coarsening however, as too low a resolution will not not capture the trends of a particular parameter within each cycle, for example the SOC curve during charging and discharging. In this study $\eta = 0.02 - 0.05$ sufficiently of captured features of the data in each cycle.

IV. GNN Training and Results

Detailed below are results from training the GNN on single cells using raw data. As the preliminary training on the dataset took upwards of 6 hours, a decision was made to run GNN training for only 100 epochs. This was done as a first pass to justify the use of such an approach to learning the degradation mechanisms at play within the battery cell. As can be seen in Figure 5, the loss substantially dropped from its original values, however prior knowledge of neural network trends suggests that another 50-100 more epochs are required to fully train the network.
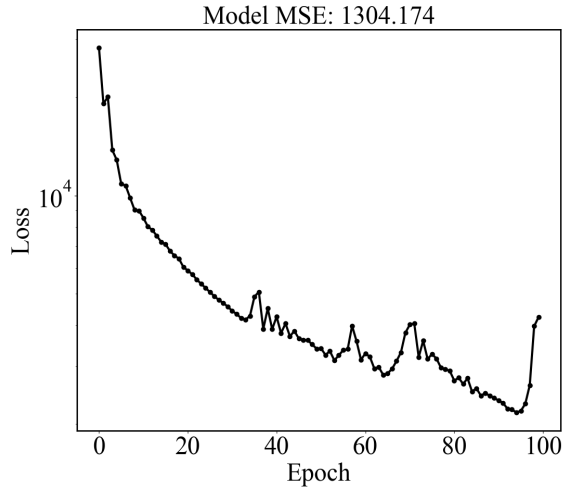

Fig. 5   **Training Loss.**

A comparison between the true and predictive values of select of the observed nodes is provided in Figure 6, except for Figure 6c in which the impact of a partially trained model was evident. First, in Figure 6a we can see that each cycle consists of a charge then a Discharge. Initial charge up to SOC = 0.8 occurs between 7.5-5 A ,then the current is decreased per the scheduling shown in Figure 7b. Figure 6c indicate the two major phase changes that occur within the NCA cathode, first at 3.5 V and secondly near 3.2V. Figure 7 portraying the behavior of select unobserved nodes of the GNN highlight the degradation behavior of key mechanisms within the cell. Shown in Figures 9a to 7c is the percentage cathode transition, SEI growth and electrolyte decomposition respectively. As these nodes were initialized to zero before training, their behavior was normalized to trends within the first few cycles. This allows us to easily rescaled the behavior given initial values from future state-of-the-art characterization techniques such as those demonstrated by Lu et. al [36]. Additionally, it must be nodes that the y-axis of the nodes indicate their relative behavior from the initial state, for example, the reverse reaction, and not necessarily a decrease in a specific quantity. Concerning cathode transition, we have a similar magnitude of behavior around the zero mean over the aging of the cell indicating that at the anode, this process does not have a significant impact on cell performance degradation. As the cell is cycled, the cathode material will continue to repeatedly undergo a phase transition with little variation with time. Note here that the behavior of the trend lines begin and end at the same value indicating the cycling behavior, but differences in slope

and data spread support the behavior of the SOC curve as shown in Figure 6a. Moreover, we can see three distinctive slopes in both the charging and discharging segments of the cycle which line up with the voltage regions at which the phase changes occur within the cell. The latter two figures suggest that most of the degradation occurs at the anode, an observation supported by literature. Charging has a significant effect on SEI growth as can be seen in Figure 9b as the behavior of SEI within the cell goes from around nominal, that is, 100 %, to nearly 300 % by the 1000 [th] cycle. This coincides with the behavior of the electrolyte decomposition as shown in Figure 7c.
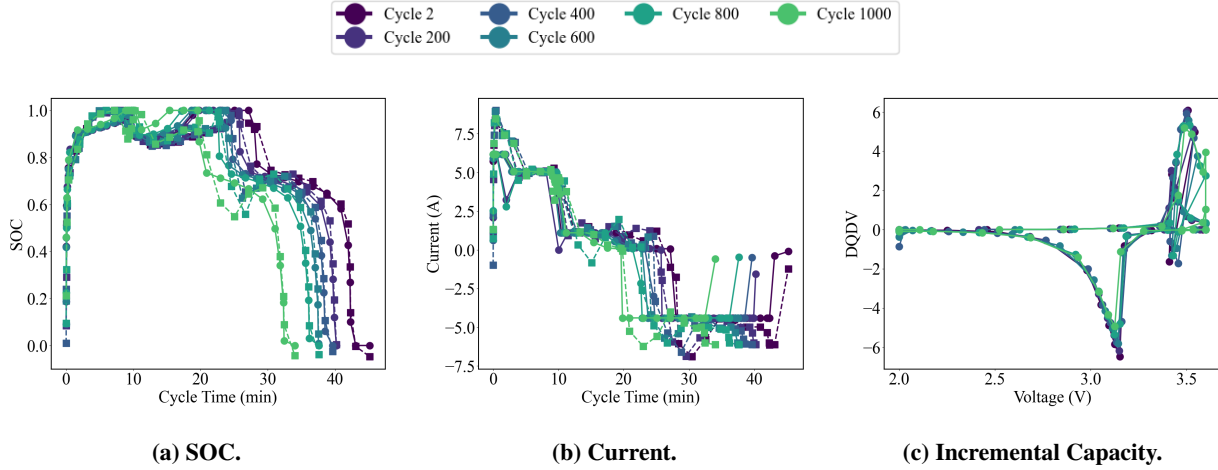

| (a) SOC. | (b) Current. | (c) Incremental Capacity. |

Fig. 6   Changes in observed graph nodes.

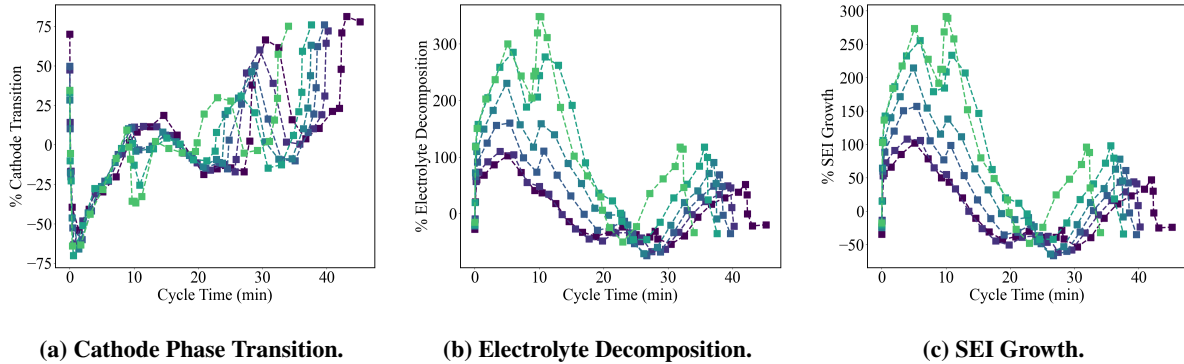| (a) Cathode Phase Transition. | (b) Electrolyte Decomposition. | (c) SEI Growth. |

Fig. 7   Relative Changes in unobserved graph nodes.

Before we discuss the behavior of trends over the entire duration of cycling, we present Figure 8 which compares two cells of differing test campaigns. Here we see that cell A has a rapid decrease in its energy storage capacity. Literature has long hypothesized reasons for this behavior. Figure 9 answers this question by providing further insight into the behavior of internal structures of the NCA cell, particularly the cathode, anode and electrolyte. The general trends within each plot show great promise and the behavior of the learned model follows precisely what is expected from literature. Again, we note here that apart from the directed nature of the graph, these nodes themselves were free to learn the model in a stochastic manner. Figure 9a supports the previously discussed trends of the cathode to undergo phase transition throughout the test campaign. The relatively constant width of the plot cycles as time progresses highlight no drastic changes in cathode behavior. On the other hand, the extent to which the decomposition of the electrolyte and reactions at the interface of the anode leading to the thickening of the SEI layer has an impact on the reduction in charge capacity is evident from Figures 9b and 9c respectively. As shown in these two diagrams, the more progressive the decomposition, the more progressive the growth of the SEI layer. This loss of electrolyte and consumption of active material is identified as the major cause of capacity degradation as previously discussed in Section II.
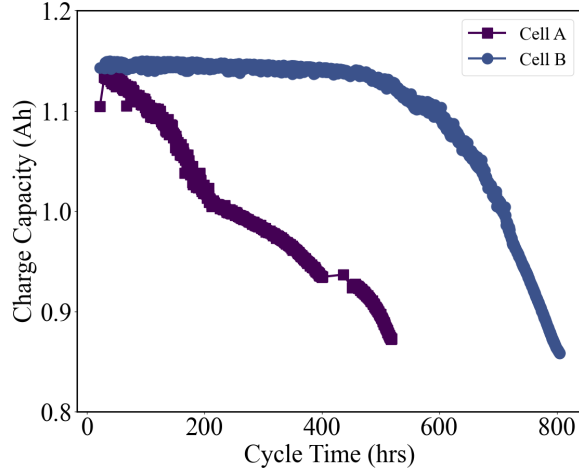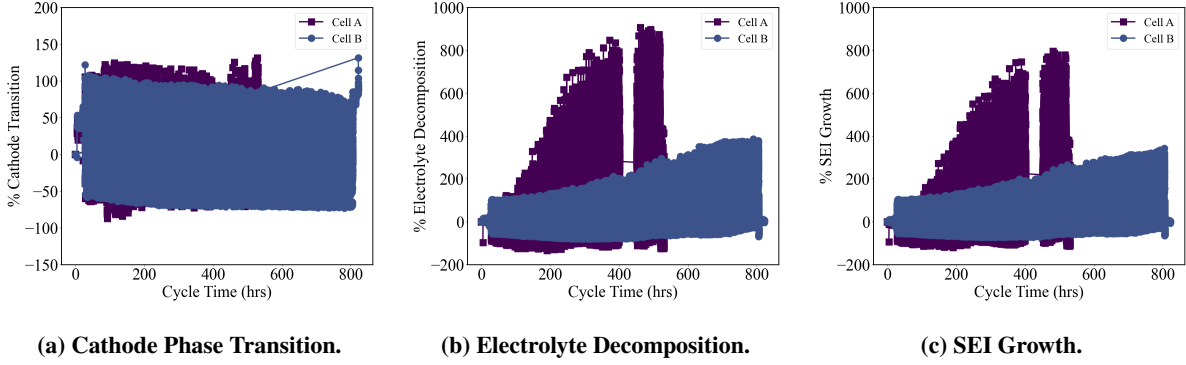
Fig. 8   Comparison of cell capacity.

(a) Cathode Phase Transition.   **(b) Electrolyte Decomposition.**   **(c) SEI Growth.**

Fig. 9   Behavior of unobserved graph nodes over test campaign.

V. Conclusions

In this paper, we present the use of a directed graph neural network with partially observed nodes to learn the behavior of degradation mechanisms with a better cell during a cycling campaign. This approach utilizes a hybrid semi-empirical model, in which known mechanistic trends of the internal structure govern information flow within the model. The preliminary results with coarsened data and shorted learning highlight promise in this approach indicated that future work should be directed towards such endeavors. This includes using more of the dataset, in terms of the resolution of the data of one cell as well as multiple cells in a batched manner to train the model, increasing the number of epochs to allow the network to reach 98% confidence and conducting additional experimental tests to validate some of the originally hidden nodes.

VI. Acknowledgements

References

[1] Doeff, M. M., "Battery Cathodes," *Batteries for Sustainability: Selected Entries from the Encyclopedia of Sustainability Science and Technology*, edited by R. J. Brodd, Springer New York, New York, NY, 2013, pp. 5–49. doi:10.1007/978-1-4614-5791-6{_}2.

[2] Purwanto, A., Yudha, C. S., Ubaidillah, U., Widiyandari, H., Ogi, T., and Haerudin, H., "NCA cathode material: Synthesis methods and performance enhancement efforts," , 9 2018. doi:10.1088/2053-1591/aae167.

[3] Ning, G., and Popov, B. N., "Cycle life modeling of lithium-ion batteries," *Journal of The Electrochemical Society*, Vol. 151, No. 10, 2004, p. A1584.

[4] Spotnitz, R., "Simulation of capacity fade in lithium-ion batteries," *Journal of power sources*, Vol. 113, No. 1, 2003, pp. 72–80.

[5] Safari, M., Morcrette, M., Teyssot, A., and Delacourt, C., "Multimodal physics-based aging model for life prediction of Li-ion batteries," *Journal of The Electrochemical Society*, Vol. 156, No. 3, 2008, p. A145.

[6] Vetter, J., Novák, P., Wagner, M. R., Veit, C., Möller, K. C., Besenhard, J. O., Winter, M., Wohlfahrt-Mehrens, M., Vogler, C., and Hammouche, A., "Ageing mechanisms in lithium-ion batteries," *Journal of Power Sources*, Vol. 147, No. 1-2, 2005, pp. 269–281. doi:10.1016/j.jpowsour.2005.01.006.

[7] Zhang, Q., and White, R. E., "Capacity fade analysis of a lithium ion cell," *Journal of Power Sources*, Vol. 179, No. 2, 2008, pp. 793–798.

[8] Ning, G., White, R. E., and Popov, B. N., "A generalized cycle life model of rechargeable Li-ion batteries," *Electrochimica acta*, Vol. 51, No. 10, 2006, pp. 2012–2022.

[9] Smith, K., Wood, E., Santhanagopalan, S., Kim, G., Neubauer, J., and Pesaran, A., "Models for battery reliability and lifetime," Tech. rep., National Renewable Energy Lab.(NREL), Golden, CO (United States), 2014.

[10] Laresgoiti, I., Käbitz, S., Ecker, M., and Sauer, D. U., "Modeling mechanical degradation in lithium ion batteries during cycling: Solid electrolyte interphase fracture," *Journal of Power Sources*, Vol. 300, 2015, pp. 112–122.

[11] Hoke, A., Brissette, A., Maksimović, D., Pratt, A., and Smith, K., "Electric vehicle charge optimization including effects of lithium-ion battery degradation," *2011 IEEE Vehicle Power and Propulsion Conference*, IEEE, 2011, pp. 1–8.

[12] Erdinc, O., Vural, B., and Uzunoglu, M., "A dynamic lithium-ion battery model considering the effects of temperature and capacity fading," *2009 International Conference on Clean Electrical Power*, IEEE, 2009, pp. 383–386.

[13] Peterson, S. B., Apt, J., and Whitacre, J., "Lithium-ion battery cell degradation resulting from realistic vehicle and vehicle-to-grid utilization," *Journal of Power Sources*, Vol. 195, No. 8, 2010, pp. 2385–2392.

[14] Koller, M., Borsche, T., Ulbig, A., and Andersson, G., "Defining a degradation cost function for optimal control of a battery energy storage system," *2013 IEEE Grenoble Conference*, IEEE, 2013, pp. 1–6.

[15] Ortega-Vazquez, M. A., "Optimal scheduling of electric vehicle charging and vehicle-to-grid services at household level including battery degradation and price uncertainty," *IET Generation, Transmission & Distribution*, Vol. 8, No. 6, 2014, pp. 1007–1016.

[16] Han, X., Lu, L., Zheng, Y., Feng, X., Li, Z., Li, J., and Ouyang, M., "A review on the key issues of the lithium ion battery degradation among the whole life cycle," *eTransportation*, Vol. 1, 2019, p. 100005. doi:10.1016/j.etran.2019.100005.

[17] Schuster, S. F., Bach, T., Fleder, E., Müller, J., Brand, M., Sextl, G., and Jossen, A., "Nonlinear aging characteristics of lithium-ion cells under different operational conditions," 2015. doi:10.1016/j.est.2015.05.003.

[18] Yang, X. G., Leng, Y., Zhang, G., Ge, S., and Wang, C. Y., "Modeling of lithium plating induced aging of lithium-ion batteries: Transition from linear to nonlinear aging," *Journal of Power Sources*, Vol. 360, 2017, pp. 28–40. doi:10.1016/j.jpowsour.2017.05.110.

[19] Park, J., Appiah, W. A., Byun, S., Jin, D., Ryou, M. H., and Lee, Y. M., "Semi-empirical long-term cycle life model coupled with an electrolyte depletion function for large-format graphite/LiFePO4 lithium-ion batteries," *Journal of Power Sources*, Vol. 365, 2017, pp. 257–265. doi:10.1016/j.jpowsour.2017.08.094.

[20] Bak, S.-m., Hu, E., Zhou, Y., Yu, X., Senanayake, S. D., Cho, S.-j., Kim, K.-b., Chung, K. Y., Yang, X.-q., and Nam, K.-w., "Structural Changes and Thermal Stability of Charged LiNi," *Applied Materials and Interfaces*, Vol. 6, No. 24, 2014, pp. 22594–22601.

11

[21] Jung, R., Metzger, M., Maglia, F., Stinner, C., and Gasteiger, H. A., "Oxygen release and its effect on the cycling stability of LiNixMnyCozO2(NMC) cathode materials for li-ion batteries," *Journal of the Electrochemical Society*, Vol. 164, No. 7, 2017, pp. A1361–A1377. doi:10.1149/2.0021707jes.

[22] Fang, R., Miao, C., Nie, Y., Wang, D., Xiao, W., Xu, M., and Wang, C., "Degradation mechanism and performance enhancement strategies of LiNixCoyAl1xyO2 (x 0.8) cathodes for rechargeable lithium-ion batteries: a review," *Ionics*, Vol. 26, No. 7, 2020, pp. 3199–3214. doi:10.1007/s11581-020-03569-7.

[23] Lin, N., Jia, Z., Wang, Z., Zhao, H., Ai, G., Song, X., Bai, Y., Battaglia, V., Sun, C., Qiao, J., Wu, K., and Liu, G., "Understanding the crack formation of graphite particles in cycled commercial lithium-ion batteries by focused ion beam - scanning electron microscopy," *Journal of Power Sources*, Vol. 365, 2017, pp. 235–239. doi:10.1016/j.jpowsour.2017.08.045.

[24] "Battery Aging and Its Influence on the Electromotive Force," 2007. doi:10.1149/1.2742296.

[25] Dubarry, M., Truchot, C., and Liaw, B. Y., "Synthesize battery degradation modes via a diagnostic and prognostic model," *Journal of Power Sources*, Vol. 219, 2012, pp. 204–216. doi:10.1016/j.jpowsour.2012.07.016.

[26] Deshpande, R., Verbrugge, M., Cheng, Y.-T., Wang, J., and Liu, P., "Battery Cycle Life Prediction with Coupled Chemical Degradation and Fatigue Mechanics," *Journal of The Electrochemical Society*, Vol. 159, No. 10, 2012, pp. A1730–A1738. doi:10.1149/2.049210jes.

[27] An, S. J., Li, J., Daniel, C., Mohanty, D., Nagpure, S., and Wood, D. L., "The state of understanding of the lithium-ion-battery graphite solid electrolyte interphase (SEI) and its relationship to formation cycling," , 8 2016. doi:10.1016/j.carbon.2016.04.008.

[28] Bak, S. M., Nam, K. W., Chang, W., Yu, X., Hu, E., Hwang, S., Stach, E. A., Kim, K. B., Chung, K. Y., and Yang, X. Q., "Correlating structural changes and gas evolution during the thermal decomposition of charged LixNi0.8Co0.15Al 0.05O2 cathode materials," *Chemistry of Materials*, Vol. 25, No. 3, 2013, pp. 337–351. doi:10.1021/cm303096e.

[29] Xu, J., Hu, E., Nordlund, D., Mehta, A., Ehrlich, S. N., Yang, X. Q., and Tong, W., "Understanding the degradation mechanism of lithium nickel oxide cathodes for Li-ion batteries," *ACS Applied Materials and Interfaces*, Vol. 8, No. 46, 2016, pp. 31677–31683. doi:10.1021/acsami.6b11111.

[30] Uitz, M., Sternad, M., Breuer, S., Täubert, C., Traußnig, T., Hennige, V., Hanzu, I., and Wilkening, M., "Aging of Tesla's 18650 Lithium-Ion Cells: Correlating Solid-Electrolyte-Interphase Evolution with Fading in Capacity and Power," *Journal of The Electrochemical Society*, Vol. 164, No. 14, 2017, pp. A3503–A3510. doi:10.1149/2.0171714jes.

[31] Rozemberczki, B., Scherer, P., He, Y., Panagopoulos, G., Riedel, A., Astefanoaei, M., Kiss, O., Beres, F., , Lopez, G., Collignon, N., and Sarkar, R., "PyTorch Geometric Temporal: Spatiotemporal Signal Processing with Neural Machine Learning Models," *Proceedings of the 30th ACM International Conference on Information and Knowledge Management*, 2021.

[32] Fey, M., and Lenssen, J. E., "Fast Graph Representation Learning with PyTorch Geometric," *ICLR Workshop on Representation Learning on Graphs and Manifolds*, 2019.

[33] Panagopoulos, G., Nikolentzos, G., and Vazirgiannis, M., "Transfer graph neural networks for pandemic forecasting," *arXiv*, 2020.

[34] Li, Y., Yu, R., Shahabi, C., and Liu, Y., "Diffusion convolutional recurrent neural network: Data-driven traffic forecasting," *6th International Conference on Learning Representations, ICLR 2018 - Conference Track Proceedings*, 2018.

[35] Graves, A., and Jaitly, N., "Towards end-to-end speech recognition with recurrent neural networks," *International conference on machine learning*, PMLR, 2014, pp. 1764–1772.

[36] Lu, J., Wu, T., and Amine, K., "State-of-the-art characterization techniques for advanced lithium-ion batteries," , No. March, 2017. doi:10.1038/nenergy.2017.11.